Classification: *Biological Sciences, Developmental Biology*

Biomechanical coupling facilitates spinal neural tube closure in mouse embryos

Short title: Biomechanics of spinal neural fold closure

Gabriel L Galea[1]*, Young-June Cho[1], Gauden Galea[2,#], Matteo A Molè[1,a], Ana Rolo[1], Dawn Savery[1], Dale Moulding[1], Lucy H Culshaw[1], Evanthia Nikolopoulou[1], Nicholas D E Greene[1], Andrew J Copp[1]

1. Newlife Birth Defects Research Centre, UCL Great Ormond Street Institute of Child Health, University College London, 30 Guilford Street, London, WC1N 1EH
2. Division of Noncommunicable Diseases and Promoting Health through the Life-course, WHO regional office for Europe, UN City, Copenhagen, Denmark, DK-2100

a. Current address: Mammalian Embryo and Stem Cell Group, University of Cambridge, Department of Physiology, Development and Neuroscience, Downing Street, Cambridge CB2 3DY, UK

\# The authors alone are responsible for the views expressed in this report and they do not necessarily represent the decisions, policy, or views of WHO or those of its Member States.

* Corresponding author: Newlife Birth Defects Research Centre, UCL Great Ormond Street Institute of Child Health, University College London, 30 Guilford Street, London, WC1N 1EH

Email: g.galea@ucl.ac.uk, Telephone: +44 7846 260 517

26   **Abstract**

27   Neural tube formation in the spinal region of the mammalian embryo involves a wave of

28   'zippering' that passes down the elongating spinal axis, uniting the neural fold tips in the

29   dorsal midline. Failure of this closure process leads to open spina bifida, a common cause of

30   severe neuro-disability in humans. Here we combined a novel tissue-level strain-mapping

31   workflow with laser ablation of live-imaged mouse embryos to investigate the biomechanics

32   of mammalian spinal closure. Ablation of the zippering point at the embryonic dorsal midline

33   causes far-reaching, rapid separation of the elevating neural folds. Strain analysis reveals

34   tissue expansion around the zippering point following ablation, but predominant tissue

35   constriction in the caudal and ventral neural plate zone. This zone is biomechanically coupled

36   to the zippering point by a supra-cellular F-actin network which includes an actin cable

37   running along the neural fold tips. Pharmacological inhibition of F-actin or laser ablation of

38   the cable causes neural fold separation. At the most advanced somite stages, when

39   completion of spinal closure is imminent, the cable forms a continuous ring around the

40   neuropore and, simultaneously, a new caudal-to-rostral zippering point arises. Laser ablation

41   of this new closure initiation point causes neural fold separation, demonstrating its

42   biomechanical activity. Failure of spinal closure in pre-spina bifida $Zic2^{Ku}$ mutant embryos is

43   associated with altered tissue biomechanics, as indicated by greater neuropore widening

44   following ablation. Thus, this study identifies biomechanical coupling of the entire region of

45   active spinal neurulation in the mouse embryo, as a pre-requisite for successful neural tube

46   closure.

47

48   **Keywords:** Neural fold, biomechanics, F-actin, Zic2, neurulation, cytoskeleton,

49   morphogenesis, strain-mapping, spina bifida, neural tube defects

50   **Significance statement:**

51   Neurulation has been intensively studied in lower vertebrates, but marked species differences

52   call into question the relevance of these models for human neural tube (NT) closure. Here,

53   using mouse embryos, we demonstrate that mammalian neural fold apposition results from

54   constriction of the open posterior NT, which is biomechanically coupled to the zippering

55   point by an F-actin network. Using the Zic2 mutant model we show that genetic

56   predisposition to spina bifida, which probably underlies most human cases, directly affects

57   the biomechanics of closure. We also identify a novel NT closure point, at the caudal end of

58   the embryo. Many spina bifida cases correspond to this anatomical portion of the NT,

59   suggesting this new closure point may be important also in humans.

60

61   \body

Introduction

Neural tube defects (NTDs) are severe neurodevelopmental disorders which affect approximately 1 in every 1,000 births (1). NTDs arise due to failure of NT closure in early gestation. In mammals, NT closure initiates at multiple sites referred to as 'closure points', with Closure 1 at the hindbrain/cervical boundary initiating cephalic and spinal neurulation. Spinal NT formation involves a wave of 'zippering' that moves in a rostral-to-caudal direction along the elongating spinal axis (2-4). The region of closing NT caudal to the 'zipper' is called the posterior neuropore (PNP). It is composed of lateral neural folds that flank a midline neural plate which caudally contains bi-potential neuromesodermal progenitors (NMPs) (5). During spinal neurulation the neural folds elevate progressively and are apposed medially, uniting at the zippering point to create the roof of the newly-formed NT covered by surface ectoderm. Failure of this closure process leads to open spina bifida (myelomeningocoele).

Failure of zippering at different somite levels results in spina bifida lesions of corresponding lengths. For example, Zic2 loss of function (*Kumba* mutant) homozygous mutant mice, in which zippering fails around the 15 somite stage, develop a large spina bifida extending from the thoracic level caudally (6). A persistent challenge in determining and ultimately preventing the developmental bases of spina bifida is the absence of a unified biomechanical understanding of the tissue deformations required for progression of NT closure. Biomechanical descriptions of vertebrate NT closure date back to the 19th century (7) and evolved in the 20th century to encompass mechanical aetiologies of NTDs described as "mechanical teratogenesis" (8). The view that abnormal tissue mechanics may underlie failure of NT closure is substantiated by experimental interventions in mouse and chick embryos in which altered ventral curvature delays or prevents completion of spinal NT closure (9, 10).

87   The demonstration that extrinsic forces can prevent NT closure implies that sufficient forces

88   are normally generated to achieve closure. However, the nature of the cellular 'motor(s)'

89   required for the initiation, progression and completion of NT closure remains incompletely

90   understood. Studies in experimentally tractable ascidians and lower vertebrates have mapped

91   mechanical stresses normally withstood within and around the neuroepithelium. This work

92   has identified cellular behaviours, such as acto-myosin-driven apical constriction of neural

93   plate cells, required to initiate apposition of the neural folds (11-16). Genetic or

94   pharmacological disruption of actin remodelling enzymes prevents NT closure in amphibians

95   as well as in mice (16-19). Moreover, progression of neurulation in mice requires

96   cytoskeleton-rich cellular protrusions from non-neural ectoderm cells directly ahead of the

97   zippering point (4, 20).

98   *In silico* simulations of amphibian embryos predict that mechanical tension within the surface

99   ectoderm and other tissues surrounding the NT serves to oppose neural fold apposition (13).

100 Indeed, tension within the non-neural ectoderm of amphibian embryos has repeatedly been

101 demonstrated by documenting immediate retraction (i.e. widening) of microsurgical incisions

102 or laser ablations (12, 21-23). However, these methods do not identify the source of tension

103 and are difficult to apply to large regions of tissue such as the PNP, which exceeds 0.6 mm in

104 length at early somite stages. Application of tensile stress to elastically deformable structures

105 (24) results in extension, leading to the structure experiencing strain (defined as the

106 percentage change in dimension). Strain can be non-invasively measured through engineering

107 techniques such as Digital Image Correlation (DIC). DIC maps the relative location of pre-

108 placed dots on the surface of structures such as bone imaged before versus after deformation

109 in order to calculate strains experienced (25, 26). Disadvantages of current DIC

110 methodologies applied to biological tissues include the requirement for a high resolution dot

111 pattern, "noisy" data due to errors in automated dot mapping, and the limitation of producing

2D/pseudo-3D analyses. Adaptations of DIC-like methodologies to biological tissues include the use of fluorescently-labelled cells as the mapped entity instead of pre-placed dots (27).

In this study we apply DIC, as well as a purpose-built Tissue Deformation and Strain Measurement (TDSM) workflow, to infer tissue stresses within and around the zippering spinal NT from the displacement of mosaic fluorescent labelled cells following mechanical disruption of the zippering point. Using these methods, together with live mouse embryo imaging, we set out to determine the role and location of the biomechanical influences that influence neural fold apposition during mouse spinal neural tube closure.

Results

Neural fold midline apposition is opposed by tension within the surrounding tissues

We initially observed that progressive narrowing of the PNP is opposed by mechanical tensions within the associated tissues. During spinal neurulation, the PNP shortens and narrows with advancing somite stage due to progressive zippering and midline apposition of the elevated neural folds (28) (Figure 1A,B). *In silico* simulations of neurulation in lower vertebrates predict neural fold midline apposition is opposed by stresses within laterally-tethering tissues (13). Consistent with this we observed that, in intact living mouse embryos, needle incision of the zippering point and most recently closed NT roof results in immediate widening of the PNP due to lateral displacement of the neural folds (Figure 1C,D, Supplementary video 1). The same effect is seen when the zippering point is laser-ablated in live-imaged embryos (Figure 1E,F). Neural fold displacement and widening of the PNP does not solely affect the ablated region, but extends more than 75% of the length of the open PNP (i.e. around 200 μm caudal to the zippering point, Figure 1G).

6

135　To infer the mechanical stresses 'withstood' by the zippering point, two methods were

136　applied to map tissue displacement and relative change in dimension ('strain', ε) within and

137　around the PNP, before versus after laser ablation of the zippering point. First, DIC was

138　implemented using two previously reported systems (Moiré DIC (29) available at

139　http://opticist.org/ and Improved DIC (30) available through MathWorks.com). We also

140　developed and applied a TDSM workflow able to quantify 3D changes in tissue dimensions

141　(SI Appendix 1 Figure 1 with further documentation in SI Appendix 2). The basis of TDSM

142　is analysis of deformation of a 3D Delaunay triangulation matrix between cell centroids

143　(Figure 2A, SI Appendix 1 Figure 1). Moiré DIC, Improved DIC and TDSM all accurately

144　quantified simulated uniaxial strains, but the latter two outperformed Moiré DIC at low strain

145　magnitudes (SI Appendix 2). Improved DIC provides von Mises strain; a measure used to

146　predict mechanical failure based on distortion energy which can be calculated independently

147　of rotation. Biological studies have previously reported area strain (percentage change in

148　area) as a similarly rotation-independent measure (31, 32). Therefore, the percentage change

149　in 2D surface area of each triangulation in the 3D mesh was used to calculate area strain in

150　TDSM (SI Appendix 2).

151　Application of TDSM to confocal stacks of live-imaged mouse embryos revealed that in

152　addition to mediolateral displacement expected from the observed PNP widening, zippering

153　point ablation also caused cells caudal to the zippering point (used as the reference point) to

154　displace in a caudo-ventral direction (Figure 2B,C). The caudo-ventral region of the PNP

155　corresponds to the location identified as containing NMPs (5) and hereafter is referred to as

156　the 'NMP zone'. Caudal displacement predominates in the open PNP whereas lateral

157　displacement is predominantly seen lateral to the zippering point and over the neural folds.

158　Caudal and lateral displacement of neuroepithelial and mesodermal cells is also apparent in

159　registered images (Figure 2D). Applying Improved DIC (Figure 3A,B) or TDSM (Figure

160   3C,D) analysis, we observed that zippering point ablation predominantly resulted in

161   expansion of the adjacent tissue and neural folds in embryos with 15-20 or 25-30 somites.

162   This was unexpected because, if the zippering point had been pulling adjacent tissue towards

163   the midline, that tissue would have been expected to relax to a smaller size (negative area

164   strain) following zippering point ablation. As a control, embryos were fixed in

165   paraformaldehyde prior to laser ablation (since fixation dissipates tissue stresses); these

166   embryos did not show significant deformations (SI Appendix 1 Figure 2).

167   Taken together, these findings suggest that progressive midline apposition of the neural folds

168   overcomes opposing mechanical tensions. Consequently, when the structural integrity of the

169   zippering point is compromised, the neural folds recoil into a more lateral position, with

170   tissue expansion and widening of the PNP.

171

172   *Constriction of the NMP zone draws the neural folds medially*

173   Strain mapping of live imaged embryos suggested that the NMP zone exists in a dynamic

174   force equilibrium with the zippering point. That is, its constriction is normally limited by the

175   tethering effect of the intact PNP, but when the zippering point is mechanically disrupted the

176   NMP zone constricts further. In contrast to expansion of tissue around the ablated zippering

177   point, a distinct region of constriction/compression was observed corresponding to the NMP

178   zone (Figure 3A-D). Compression of the caudo-ventral PNP following zippering point

179   ablation was confirmed using a more targeted Cre driver (Nkx1-2, Figure 3E) and selective

180   TDSM analysis of this zone (Figure 3F). This avoided confounding effects of surrounding

181   tissues extending towards it. Regional area strain analyses confirmed significant expansion of

182   tissue rostral to the zippering point and significant compression of tissue caudal to it (SI

183   Appendix 1 Figure 2B). Hence, ablation of the zippering point causes far-reaching

184   deformation, suggesting that the zippering point is biomechanically coupled to the NMP

185   zone.

186   In order to visualise these dynamic behaviours, a system of medium-term live embryo

187   imaging was developed which allows analysis of changes in cellular apical surface area as

188   well as observation of continued apposition of the neural folds (Figure 4A). Apical surface

189   area of NMP zone cells decreased relative to their initial size over an hour of live imaging

190   (Figure 4B), documenting in mammalian embryos a process which has been found to

191   biomechanically mediate neural fold midline approximation in lower vertebrates (14, 19, 33).

192   The surface area of surface ectoderm cells immediately rostral to the zippering point did not

193   change significantly over the same time-frame (SI Appendix 1 Figure 3A,B). Overall PNP

194   length tended to decrease over the time-frame analysed, with occasional observation of

195   zippering point cellular protrusions consistent with ongoing closure (SI Appendix 1 Figure

196   3C,D). Medial apposition of the neural folds resulted in a significant reduction in PNP width

197   and in the zippering point angle (Figure 4C,D). Dorsoventral cell displacement, as a potential

198   basis for PNP narrowing, was found to be minimal over the same time-frame (SI Appendix 1

199   Figure 4).

200   Taken together, strain mapping and live imaging analysis suggest that the continuation of

201   PNP closure is associated with selective constriction of NMP zone cells, aiding the apposition

202   of the neural folds in the midline, and thereby narrowing the zippering point angle across

203   which cellular protrusions must reach.

204

205   *A long-ranging F-actin network biomechanically couples the posterior neuropore*

206   We found that biomechanical coupling of the zippering point to the NMP zone involves a

207   supracellular F-actin network extending between these structures. In mouse embryos, apical

208 actomyosin enrichment has previously been documented in the NMP zone ((17) and SI

209 Appendix 1 Figure 5A) as well as in the neuroepithelium of the closing NT (34). Whole-

210 mount imaging of phalloidin-stained mouse embryos confirmed the presence of a dense F-

211 actin network in the NMP zone and revealed the presence of a long F-actin cable emanating

212 from the zippering point and running caudally along the neural folds (Figure 5A, SI

213 Appendix 1 Figure 5B). This cable colocalised with the surface ectoderm adherens junction

214 marker E-cadherin at the surface ectoderm/neuroepithelial boundary (Figure 5B), forming a

215 continuous structure across cell junctions (SI Appendix 1 Figure 5B).

216 In embryos at early somite stages with long PNPs, the cable could be over 0.5 mm in length,

217 and yet did not fully encircle the PNP (Figure 5A). At later stages, when the PNP had

218 shortened to a length of less than ~ 300 μm (SI Appendix 1 Figure 6A-D), the cable encircled

219 the PNP forming an elongated 'purse string'-like structure (Figure 5C). This association

220 between cable length and PNP length held true in embryos from wild-type mice maintained

221 on three different background strains (SI Appendix 1 Figure 6). The transition to the F-actin

222 cable encircling the PNP is marked by a dramatic change in PNP shape distally, from an early

223 'spade-like' structure to a late-stage elliptical structure. F-actin staining revealed enrichment

224 at both the zippering point and at the caudal-most PNP canthus in late-stage PNPs (Figure

225 5C). Moreover, scanning electron microscopy detected cellular protrusions (20) at both sites

226 (Figure 5D). This suggests that, when completion of closure is imminent, a new zippering

227 point forms at the caudal extremity of the PNP.

228

229 *A novel caudal closure point forms when completion of spinal neurulation is imminent*

230 The caudal canthus of the late-stage PNP biomechanically facilitates neural fold apposition.

231 We refer to this novel caudal closure point as 'Closure 5' (cyan arrow in Figure 5C): it was

232 previously hypothesised to exist in mice based on the morphology of late-stage PNPs (35), as

233 well as in humans based on the distribution of spina bifida lesions (36, 37), but its existence

234 has never been conclusively demonstrated. To determine whether Closure 5 contributes to

235 neural fold apposition, it was laser-ablated in live-imaged 25-30 somite mouse embryos.

236 Ablation of the F-actin ring at Closure 5 resulted in widening of the PNP, as did ablation of

237 the ring at the rostral PNP zippering point (Figure 6A,C-E). In contrast, ablation of the caudal

238 tip of the PNP in 15-20 somite embryos, before the formation of Closure 5, did not result in

239 significant PNP widening, whereas ablating the F-actin cable at the zippering point or along

240 the neural folds did result in widening of the PNP (Figure 6D). We hypothesised that the

241 observed PNP widening following ablation of the zippering point, Closure 5 or along the

242 neural folds related to disruption of the F-actin network. To test this further, actin was acutely

243 inhibited by 15 mins treatment with Latrunculin B (LatB), which resulted in dose-dependent

244 PNP widening (SI Appendix 1 Figure 7).

245 Thus, the F-actin network biomechanically couples the PNP and facilitates drawing of the

246 neural folds towards the midline such that ablating the F-actin cable at the zippering point,

247 along the neural folds, or at Closure 5, or pharmacologically severing F-actin with LatB, in

248 each case results in the neural folds moving apart such that the PNP widens.

249

250 *The biomechanics of neural fold apposition are altered by mutations in Zic2*

251 Altered biomechanics may underlie faulty neural tube closure in a mouse model of severe

252 spina bifida. This was inferred from the change in PNP width observed following zippering

253 point ablation in *Kumba* (*Zic2^{Ku}*) mutants, which carry a functionally null allele of the

254 transcription factor Zic2 (38). *Zic2$^{Ku/Ku}$* embryos show dramatically enlarged PNPs with

255 100% penetrance at late neurulation stages, but at the 12-15 somite stage total PNP length is

256 not yet significantly altered (representative examples in Figure 7A). At this stage the F-actin

257 cable is clearly visible along the neural folds in $Zic2^{+/+}$ and $Zic2^{Ku/+}$, whereas in $Zic2^{Ku/Ku}$

258 embryos only short segments of this cable are visible (Figure 7A). PNP widening is observed

259 in all three genotypes following laser ablation of the zippering point, but widening was

260 significantly greater in $Zic2^{Ku/Ku}$ embryos than in wild-type littermates, particularly just

261 caudal to the zippering point (Figure 7B). Greater PNP widening in $Zic2^{Ku/Ku}$ compared with

262 $Zic2^{+/+}$ embryos was also observed following microsurgical incision of the zippering point

263 (SI Appendix 1 Figure 8). $Zic2^{Ku/+}$ embryos, which do successfully close their PNP, undergo

264 significantly greater widening than $Zic2^{+/+}$ littermates at various points along the open PNP.

265 These observations suggest that genetically-influenced alterations in the biomechanics of

266 spinal closure may underlie spina bifida in this mammalian model.

267

Discussion

269 Mammalian spinal neurulation is a biomechanical event requiring midline apposition of the

270 neural folds, narrowing the PNP as it shortens through zippering. Inference of cellular

271 biomechanics by laser ablation in simpler organisms is well-established (11, 39-42), but is

272 substantially complicated in mouse embryos by their comparatively large size, complex shape

273 and tissue opacity. Here we investigated effects of needle and laser ablations on tissue

274 morphology many cell diameters away from the ablation site in live imaged embryos. These

275 studies demonstrate that the mammalian PNP is a biomechanically coupled structure (Figure

276 7C) in which neural fold medial apposition is aided by constriction of the caudo-ventral NMP

277 zone, narrowing the rostral zippering point angle across which cellular protrusions must reach

278 and facilitating the progression of closure.

279 The closing PNP progressively shortens and narrows with advancing somite stage, and the

280 zippering point is critically involved in PNP shortening, as genetic disruption of surface

281 ectoderm cellular protrusions normally formed at this point prevents completion of closure

282 (20, 43). Here we show that the zippering point also serves a biomechanical function as its

283 physical ablation results in rapid lateral displacement of the neural folds, widening the PNP.

284 Biomechanically-active components involved in neural tube formation have primarily been

285 studied in *Xenopus*, in which apical constriction has been implicated in bending of the bi-

286 layered neuroepithelium (14, 19, 44). Actomyosin contraction is an evolutionarily conserved

287 force-generating mechanism, with resulting forces transmitted between biomechanically

288 coupled cells primarily through cadherin/catenin adherens junctions (45, 46).

289 The marked apical enrichment of actomyosin that we observe in NMP zone cells is consistent

290 with apical constriction of these cells aiding medial apposition of the neural folds towards the

291 midline as a biomechanically coupled unit. We have demonstrated that biomechanical

292 coupling of the mammalian PNP involves a long-range F-actin cable which extends from the

293 zippering point rostrally, runs along the neural folds as a continuous structure across cell-cell

294 junctions where it co-localises with E-cadherin, and joins the apically-enriched actomyosin

295 network of the NMP zone cells caudally. All of the functional landmarks laser ablated in this

296 study which involve the F-actin cable resulted in PNP widening. Similar tension bearing F-

297 actin cables or rings form during zebrafish epiboly (47), chick amniogenesis (48) mouse

298 eyelid closure (49, 50), and during *Drosophila* dorsal closure (51, 52), suggesting they are an

299 evolutionarily conserved mechanism of transmitting forces across many cell diameters.

300 The findings of this study suggest that the cellular programmes underlying PNP 'narrowing,'

301 which is enhanced by apical constriction in the NMP zone, are likely to be distinct from those

302 regulating surface ectoderm-mediated cellular protrusions required for PNP 'shortening' (20,

303 43). In support of this idea, we recently found that preventing actin turnover abrogates

304 progression of mouse PNP closure whereas treatment with actomyosin inhibitors, at

305 concentrations compatible with continued development in culture, does not significantly

13

306 delay zippering (17, 53). Indeed, as different cell types (neural versus surface ectoderm) are

307 primarily involved in PNP narrowing and shortening, it seems reasonable that they may be

308 susceptible to different genetic or environmental impediments, leading to spina bifida through

309 distinct mechanisms.

310 Clustered cases of distal lumbosacral spina bifida observed in human patients (36) have led to

311 the suggestion that a final closure initiation point may be involved in completion of PNP

312 closure. This final closure has been referred to as the "fourth fusion" (35) or "Closure 5" (36),

313 but its existence has not been experimentally demonstrated in any mammal (54). In the

314 present study, we found that the caudal canthus of the PNP forms a new zippering structure

315 that is not only characterised by cellular protrusions, which typify the main zippering point

316 (20), but also functionally contributes to late PNP narrowing, as its disruption by laser

317 ablation results in re-widening of the PNP. Hence, this work provides the first functional

318 evidence for an active closure mechanism at the caudal extremity, Closure 5, which arises

319 late in spinal neurulation.

320 A limitation of the short-term interventions described here is that their consequences for

321 continuation of spinal closure could not be directly investigated. For this reason we studied

322 the $Zic2^{Ku/Ku}$ mutant, a well-characterised genetic model in which homozygous mutants

323 develop spina bifida, whereas heterozygous embryos achieve closure in most cases (38). A

324 mechanical basis for spina bifida in the $Zic^{Ku/Ku}$ mutant had previously been suggested as

325 these embryos display neural folds that fail to bend towards the midline at dorsolateral hinge

326 points (6). We observed that the F-actin cable appeared fragmented in $Zic2^{Ku/Ku}$ mutants,

327 which is consistent with a previous report that morpholino-mediated knockdown of Zic

328 transcription factors in zebrafish disrupts the contiguous actomyosin "apical seam" which

329 normally forms along the presumptive hindbrain lumen (55). Failure of spinal closure in the

330 $Zic2^{Ku/Ku}$ mutant was found to be associated with altered PNP biomechanics, resulting in a

331 greater magnitude of PNP re-widening following zippering point ablation. The cellular basis

332 of the altered PNP biomechanics in the Zic2 mutant embryos is currently unknown, although

333 the observation that Zic2 is expressed almost solely in the neuroepithelium during spinal

334 neurulation (6) suggests that a neuroepithelial defect is likely to be responsible.

335 In conclusion, spinal NT closure in the mouse embryo is facilitated by apical constriction of

336 cells within the NMP zone to which the neural folds are biomechanically coupled by an

337 extensive actomyosin network (Figure 6C), including an F-actin cable that demarcates the

338 boundary between the PNP and the E-cadherin expressing surface ectoderm. This

339 biomechanical coupling is genetically influenced at least in part by activity of Zic2. We

340 therefore propose that genetically-influenced biomechanical morphogenetic disorders may be

341 an important cause of spina bifida.

342

343 **Materials and Methods**

344 *Animal procedures*

345 Studies were performed under project license number 70/7469 under the UK Animals

346 (Scientific Procedures) Act 1986 and the Medical Research Council's Responsibility in the

347 Use of Animals for Medical Research (1993). Mice were time-mated overnight and the

348 morning a copulation plug was identified was considered E0.5. Heterozygous $Grhl3^{Cre}$, $Nkx1$-

349 $2^{CreERT2}$ and β-$actin^{CreERT2}$ were as previously described (20, 56-58) and were maintained on a

350 C57BL/6 background. ERT2 activity was induced by intraperitoneal injection of 0.2 mg/40 g

351 body weight of tamoxifen (Sigma) at E8.5. To generate mosaic fluorescent cell patterns in the

352 PNP, heterozygous Cre-expressing mice were crossed with homozygous ROSA26-EYFP (20)

353 or mTmG mice (59). Cre-negative mice were used for studies requiring non-transgenic mice.

354 $Zic2^{Ku}$ mutants and their genotyping were as previously described (6).

355

Embryo dissection and pharmacological treatment

357   Embryos were harvested around E9.5 as previously described (60). For whole mount,

358   embryos were dissected and rinsed in PBS prior to fixation in 4% paraformaldehyde, pH 7.4.

359   For LatB (Sigma) treatments, embryos were fully dissected from the amnion and pre-warmed

360   for 30 mins in DMEM containing 10% fetal bovine serum prior to addition of LatB or DMSO

361   vehicle and fixed after 15 mins of treatment. Fixed embryos were stained with CellMask™

362   Green (Thermo Fisher Scientific) and their PNPs were imaged on a fluorescence stereo

363   microscope (Leica MZ FIII, DC500 camera). PNP mid-point widths were analysed in ImageJ

364   (NIH (61)).

365

Laser ablation and live embryo imaging

367   For ablations, embryos were dissected from the amnion, positioned in wells cut out of 4%

368   agarose gel in DMEM, submerged in dissection medium and maintained at 37°C throughout

369   imaging. Microsurgical needles from 11-0 Mersilene (TG140-6, Ethicon) and 10-0 Prolene

370   (BV75-3, Ethicon) were used to hold the embryos in place with the PNP pointing upwards

371   while minimising contact with the heart, which continued to beat steadily throughout each

372   experiment. Images were captured on a Zeiss Examiner LSM880 confocal using a 20x/NA1.0

373   Plan Apochromat dipping objective. If intended for strain mapping, embryos were imaged

374   with X/Y pixel sizes of 0.59 μm and Z-step of 1.0 μm, taking approximately 7-10 minutes to

375   image a PNP (speed = 8, bidirectional imaging, 1024 x 1024 pixels). To measure PNP widths

376   without strain mapping, embryos were typically imaged with X/Y pixel sizes of 1.2 μm and

377   Z-step of 2.4 μm, taking approximately 2-4 minutes to image a single PNP using reflection

378   mode (MBS T80/R20 beam filter). Before and after ablation images for each embryo were

379 captured using the same settings. Resulting Z-stacks were re-oriented and resliced in Imaris

380 (Version 8), minimizing changes due to drift or embryo movement between Z stacks.

381 Laser ablations were performed on the Zeiss Examiner LSM880 confocal microscope using a

382 20x/NA1.0 Plan Apochromat dipping objective and a MaiTai laser (SpectraPhysics Mai Tai

383 eHP DeepSee multiphoton laser, 800 nm wavelength, 100% laser power, 65.94 μs pixel dwell

384 time, 0.83 μs pixel size, 1 iteration). A 300-500 μm line of closed NT roof was ablated along

385 the embryonic midline by ablating each section within the focal plane. Ablation instantly

386 vaporised a narrow region of tissue, as previously described in mouse embryos (62).

387 For live imaging, embryos were dissected in an intact yolk sac as for long term embryo

388 culture (60) and positioned in agarose wells as described above. A small window was made

389 in a minimally vascular part of the yolk sac and the amnion over the PNP was removed to

390 allow direct visualisation of the PNP. All embryos were kept at 37°C in neat rat serum

391 exposed to 5% CO_2/5%N_2 in air in a custom-made chamber (Solent Scientific) humidified

392 with damp cotton wool. PNPs were imaged with X/Y pixel sizes 0.59 μm and Z-step of 2.5

393 μm, taking approximately 10 minutes to image each PNP. All embryos had a normal heart

394 beat and yolk sac circulation throughout imaging.

395

396 *Whole mount staining*

397 All images are representative of observations in at least three independent embryos. Scanning

398 electron microscopy was performed as in (20). Mouse anti-E-cadherin antibody (BD

399 Transduction Laboratories), rabbit anti-pMLCII (Ser19, Cell Signalling), mouse anti-total β-

400 catenin (Santa Cruz) and Alexa Fluor®-568 conjugated phalloidin (Life Technologies) were

401 used. Paraformaldehyde-fixed embryos were permeabilised in PBS with 0.1% Triton X-100

402 (PBT) for 1 hr at room temperature, blocked overnight in a 5% BSA/PBT at 4°C and

403   incubated overnight in a 1:150 dilution of primary antibody in blocking solution at 4°C.

404   Embryos were then washed 3 x 1 hr at room temperature in blocking solution, incubated for 2

405   hrs at room temperature in 1:300 dilution of Alexa Fluor®-conjugated secondary antibodies

406   (Thermo Fisher Scientific), 1:200 dilution of phalloidin and 0.5 μg/ml DAPI in blocking

407   solution. Excess secondary antibody was removed by washing for 1 hr in blocking solution

408   and a further 2 x 1 hr in PBT at room temperature. Stained embryos were imaged on a Zeiss

409   Examiner LSM880 confocal microscope. High resolution images in SI Appendix 1 Figure 5B

410   were taken using Airyscan in SR mode, 2x zoom, with optimal pixel size and z step (XY

411   pixel size 0.065 μm, Z step 0.36 μm). Alexa 568 fluorescence from 570 to 620 nm was

412   collected through a LP570 secondary beam splitter and the Airyscan filter wheel with a

413   BP495-620. Images were processed with Zen2.3 software using auto Airyscan processing.

414

415   *Strain mapping*

416   Application of DIC was according to the software authors' instructions and is described

417   further in SI Appendix 2. Application of TDSM is described in further detail in SI Appendix

418   2. In brief, live imaged PNPs before and after zippering point ablation were digitally resliced

419   in Imaris (version 8) to ensure equivalent positioning and the ImageJ 3D object counter was

420   used to map cell centroids. The X/Y/Z centroids of cells identified in both 'before' and 'after'

421   images were exported to TDSM, which describes Delaunay triangulations between the same

422   centroids before and after ablation with the zippering point normalised to the graph origin.

423   The percentage change in 2D area of each Delaunay triangle in the 3D meshwork was then

424   calculated. Heat maps were generated in OriginPro 2016 (Origin Labs) as the aggregate of

425   data from three independent embryos in each group.

426   Strain maps were generated using three Cre drivers. Grhl3Cre is mosaic in the mesoderm and

427   neuroepithelium but ubiquitous in the surface ectoderm: strain maps generated using this

428   driver only include mesodermal and neuroepithelial cells. β-actin Cre^{ERT2} was induced at a

429   low recombination rate in all cell types. Nkx1-2 Cre^{ERT2} lineage-traces both mesodermal and

430   neuroepithelial cell types, but only cells within the caudo-ventral PNP with a neuroepithelial

431   morphology were analysed. Imaging depth was around 100 μm from the surface such that

432   strain maps represent cells up to 100 μm deep into the tissue.

433

434   *Statistical analysis*

435   Comparisons between two groups were by Student's unpaired t-test accounting for

436   homogeneity of variance in Excel or in SPSS (IBM Statistics 22). Comparison of multiple

437   groups was by one-way ANOVA with post-hoc Bonferroni in SPSS. Linear regression was in

438   OriginPro 2016 (Origin Labs). Multivariate analysis was by linear mixed models in SPSS

439   accounting for the fixed effects of genotype, time or distance from the zippering point in

440   repeated measures from each embryo (random variable) as appropriate for the analysis, with a

441   post-hoc Bonferroni where applicable. Analysis of PNP widening in the *Kumba* embryos was

442   performed blind prior to genotyping. Graphs were made in OriginPro 2016 (Origin Labs) and

443   are represented as raw data point or box plots when single groups are shown per

444   measurement level, or as the mean ± SEM when several groups are shown per measurement

445   level. $P < 0.05$ was considered statistically significant.

446

455

456 **Conflict of Interest Statement:** The authors have declared that no conflict of interest exists.

457

458 **Author contributions:**

459 GLG, AJC, NDEG and AR designed the study and provided reagents. GLG performed and

460 analysed the experiments with help from DM (microscopy and laser ablation), MAM (live

461 imaging), EN and LC (whole mount staining) and YJC (micro-surgical incisions and DiI

462 labelling). AR produced the SEM images. GG scripted TDSM and GLG produced the

463 validation documents. DS managed the mouse colonies. GLG, AJC and NG wrote the

464 manuscript with contributions from all authors.

465

References:

1. Morris JK, *et al.* (2016) Prevention of neural tube defects in the UK: a missed opportunity. *Archives of disease in childhood* 101(7):604-607.
2. Van Straaten HW, Janssen HC, Peeters MC, Copp AJ, & Hekking JW (1996) Neural tube closure in the chick embryo is multiphasic. *Developmental dynamics : an official publication of the American Association of Anatomists* 207(3):309-318.
3. van Straaten HW, Peeters MC, Hekking JW, & van der Lende T (2000) Neurulation in the pig embryo. *Anatomy and embryology* 202(2):75-84.
4. Ray HJ & Niswander LA (2016) Dynamic behaviors of the non-neural ectoderm during mammalian cranial neural tube closure. *Developmental biology* 416(2):279-285.
5. Henrique D, Abranches E, Verrier L, & Storey KG (2015) Neuromesodermal progenitors and the making of the spinal cord. *Development* 142(17):2864-2875.
6. Ybot-Gonzalez P, *et al.* (2007) Neural plate morphogenesis during mouse neurulation is regulated by antagonism of Bmp signalling. *Development* 134(17):3203-3211.
7. His W (1894) Über mechanische Grundvorgänge thierischer Formbildung [On the mechanical basis of animal morphogenesis]. *Arch Anat Physiol u wiss Med: Anat Abth*:1-80.
8. Miller ME, Graham JM, Jr., Higginbottom MC, & Smith DW (1981) Compression-related defects from early amnion rupture: evidence for mechanical teratogenesis. *The Journal of pediatrics* 98(2):292-297.
9. Brook FA, Shum AS, Van Straaten HW, & Copp AJ (1991) Curvature of the caudal region is responsible for failure of neural tube closure in the curly tail (ct) mouse embryo. *Development* 113(2):671-678.
10. van Straaten HW, Hekking JW, Consten C, & Copp AJ (1993) Intrinsic and extrinsic factors in the mechanism of neurulation: effect of curvature of the body axis on closure of the posterior neuropore. *Development* 117(3):1163-1172.
11. Hashimoto H, Robin FB, Sherrard KM, & Munro EM (2015) Sequential contraction and exchange of apical junctions drives zippering and neural tube closure in a simple chordate. *Developmental cell* 32(2):241-255.
12. Benko R & Brodland GW (2007) Measurement of in vivo stress resultants in neurulation-stage amphibian embryos. *Annals of biomedical engineering* 35(4):672-681.
13. Brodland GW, Chen X, Lee P, & Marsden M (2010) From genes to neural tube defects (NTDs): insights from multiscale computational modeling. *HFSP journal* 4(3-4):142-152.
14. Inoue Y, *et al.* (2016) Mechanical roles of apical constriction, cell elongation, and cell migration during neural tube formation in Xenopus. *Biomechanics and modeling in mechanobiology*.
15. Sokol SY (2016) Mechanotransduction During Vertebrate Neurulation. *Current topics in developmental biology* 117:359-376.
16. Vijayraghavan DS & Davidson LA (2016) Mechanics of neurulation: From classical to current perspectives on the physical mechanics that shape, fold, and form the neural tube. *Birth defects research. Part A, Clinical and molecular teratology*.
17. Escuin S, *et al.* (2015) Rho-kinase-dependent actin turnover and actomyosin disassembly are necessary for mouse spinal neural tube closure. *Journal of cell science* 128(14):2468-2481.
18. Grego-Bessa J, Hildebrand J, & Anderson KV (2015) Morphogenesis of the mouse neural plate depends on distinct roles of cofilin 1 in apical and basal epithelial domains. *Development* 142(7):1305-1314.
19. Ossipova O, *et al.* (2014) Role of Rab11 in planar cell polarity and apical constriction during vertebrate neural tube closure. *Nature communications* 5:3734.
20. Rolo A, *et al.* (2016) Regulation of cell protrusions by small GTPases during fusion of the neural folds. *eLife* 5:e13273.
21. Lewis WH (1947) Mechanics of invagination. *The Anatomical record* 97(2):139-156.

516   22.   Jacobson AG & Gordon R (1976) Changes in the shape of the developing vertebrate nervous
517   system analyzed experimentally, mathematically and by computer simulation. *The Journal of*
518   *experimental zoology* 197(2):191-246.
519   23.   Morita H*, et al.* (2012) Cell movements of the deep layer of non-neural ectoderm underlie
520   complete neural tube closure in Xenopus. *Development* 139(8):1417-1426.
521   24.   Beloussov LV, Dorfman JG, & Cherdantzev VG (1975) Mechanical stresses and morphological
522   patterns in amphibian embryos. *Journal of embryology and experimental morphology*
523   34(3):559-574.
524   25.   Carriero A, Abela L, Pitsillides AA, & Shefelbine SJ (2014) Ex vivo determination of bone
525   tissue strains for an in vivo mouse tibial loading model. *Journal of biomechanics* 47(10):2490-
526   2497.
527   26.   Begonia MT*, et al.* (2015) Non-contact strain measurement in the mouse forearm loading
528   model using digital image correlation (DIC). *Bone* 81:593-601.
529   27.   Khodabakhshi G*, et al.* (2013) Measuring three-dimensional strain distribution in tendon.
530   *Journal of microscopy* 249(3):195-205.
531   28.   van Straaten HW, Hekking JW, Copp AJ, & Bernfield M (1992) Deceleration and acceleration
532   in the rate of posterior neuropore closure during neurulation in the curly tail (ct) mouse
533   embryo. *Anatomy and embryology* 185(2):169-174.
534   29.   Wang Z, Kieu H, Nguyen H, & Le M (2015) Digital image correlation in experimental
535   mechanics and image registration in computer vision: Similarities, differences and
536   complements. *Optics and Lasers in Engineering* 65:18-27.
537   30.   Jones EMC, Silberstein MN, White SR, & Sottos NR (2014) In Situ Measurements of Strains in
538   Composite Battery Electrodes during Electrochemical Cycling. *Experimental Mechanics*
539   54(6):971-985.
540   31.   Li F, Chan CU, & Ohl CD (2013) Yield strength of human erythrocyte membranes to impulsive
541   stretching. *Biophysical journal* 105(4):872-879.
542   32.   Yuan F, Yang C, & Zhong P (2015) Cell membrane deformation and bioeffects produced by
543   tandem bubble-induced jetting flow. *Proceedings of the National Academy of Sciences of the*
544   *United States of America* 112(51):E7039-7047.
545   33.   Rolo A, Skoglund P, & Keller R (2009) Morphogenetic movements driving neural tube closure
546   in Xenopus require myosin IIB. *Developmental biology* 327(2):327-338.
547   34.   Sadler TW, Greenberg D, Coughlin P, & Lessard JL (1982) Actin distribution patterns in the
548   mouse neural tube during neurulation. *Science* 215(4529):172-174.
549   35.   Sakai Y (1989) Neurulation in the mouse: manner and timing of neural tube closure. *The*
550   *Anatomical record* 223(2):194-203.
551   36.   Van Allen MI*, et al.* (1993) Evidence for multi-site closure of the neural tube in humans.
552   *American journal of medical genetics* 47(5):723-743.
553   37.   Seller MJ (1995) Further evidence for an intermittent pattern of neural tube closure in
554   humans. *Journal of medical genetics* 32(3):205-207.
555   38.   Elms P, Siggers P, Napper D, Greenfield A, & Arkell R (2003) Zic2 is required for neural crest
556   formation and hindbrain patterning during mouse development. *Developmental biology*
557   264(2):391-406.
558   39.   Shivakumar PC & Lenne PF (2016) Laser Ablation to Probe the Epithelial Mechanics in
559   Drosophila. *Methods in molecular biology* 1478:241-251.
560   40.   Vogel A & Venugopalan V (2003) Mechanisms of pulsed laser ablation of biological tissues.
561   *Chemical reviews* 103(2):577-644.
562   41.   Keller R, Davidson LA, & Shook DR (2003) How we are shaped: the biomechanics of
563   gastrulation. *Differentiation; research in biological diversity* 71(3):171-205.
564   42.   Hardin J (1988) The role of secondary mesenchyme cells during sea urchin gastrulation
565   studied by laser ablation. *Development* 103(2):317-324.

566 43. Rolo A, Escuin S, Greene ND, & Copp AJ (2016) Rho GTPases in mammalian spinal neural
567   tube closure. *Small GTPases*:1-7.
568 44. Christodoulou N & Skourides PA (2015) Cell-Autonomous Ca(2+) Flashes Elicit Pulsed
569   Contractions of an Apical Actin Network to Drive Apical Constriction during Neural Tube
570   Closure. *Cell reports* 13(10):2189-2202.
571 45. Heisenberg CP & Bellaiche Y (2013) Forces in tissue morphogenesis and patterning. *Cell*
572   153(5):948-962.
573 46. Vasquez CG & Martin AC (2016) Force transmission in epithelial tissues. *Developmental*
574   *dynamics : an official publication of the American Association of Anatomists* 245(3):361-371.
575 47. Chai J*, et al.* (2015) A force balance can explain local and global cell movements during early
576   zebrafish development. *Biophysical journal* 109(2):407-414.
577 48. Tipping N & Wilson D (2011) Chick amniogenesis is mediated by an actin cable. *Anatomical*
578   *record* 294(7):1143-1149.
579 49. Hislop NR*, et al.* (2008) Grhl3 and Lmo4 play coordinate roles in epidermal migration.
580   *Developmental biology* 321(1):263-272.
581 50. Heller E, Kumar KV, Grill SW, & Fuchs E (2014) Forces generated by cell intercalation tow
582   epidermal sheets in mammalian tissue morphogenesis. *Developmental cell* 28(6):617-632.
583 51. Pasakarnis L, Frei E, Caussinus E, Affolter M, & Brunner D (2016) Amnioserosa cell
584   constriction but not epidermal actin cable tension autonomously drives dorsal closure.
585   *Nature cell biology* 18(11):1161-1172.
586 52. Ducuing A & Vincent S (2016) The actin cable is dispensable in directing dorsal closure
587   dynamics but neutralizes mechanical stress to prevent scarring in the Drosophila embryo.
588   *Nature cell biology* 18(11):1149-1160.
589 53. Ybot-Gonzalez P & Copp AJ (1999) Bending of the neural plate during mouse spinal
590   neurulation is independent of actin microfilaments. *Developmental dynamics : an official*
591   *publication of the American Association of Anatomists* 215(3):273-283.
592 54. Copp AJ, Stanier P, & Greene ND (2013) Neural tube defects: recent advances, unsolved
593   questions, and controversies. *The Lancet. Neurology* 12(8):799-810.
594 55. Nyholm MK, Abdelilah-Seyfried S, & Grinblat Y (2009) A novel genetic mechanism regulates
595   dorsolateral hinge-point formation during zebrafish cranial neurulation. *Journal of cell*
596   *science* 122(Pt 12):2137-2148.
597 56. Lewandoski M & Martin GR (1997) Cre-mediated chromosome loss in mice. *Nature genetics*
598   17(2):223-225.
599 57. Camerer E*, et al.* (2010) Local protease signaling contributes to neural tube closure in the
600   mouse embryo. *Developmental cell* 18(1):25-38.
601 58. Rodrigo Albors A, Halley PA, & Storey KG (2016) Fate mapping caudal lateral epiblast reveals
602   continuous contribution to neural and mesodermal lineages and the origin of secondary
603   neural tube. *bioRxiv*.
604 59. Muzumdar MD, Tasic B, Miyamichi K, Li L, & Luo L (2007) A global double-fluorescent Cre
605   reporter mouse. *Genesis* 45(9):593-605.
606 60. Pryor SE, Massa V, Savery D, Greene ND, & Copp AJ (2012) Convergent extension analysis in
607   mouse whole embryo culture. *Methods in molecular biology* 839:133-146.
608 61. Schindelin J*, et al.* (2012) Fiji: an open-source platform for biological-image analysis. *Nature*
609   *methods* 9(7):676-682.
610 62. Angelo JR & Tremblay KD (2013) Laser-mediated cell ablation during post-implantation
611   mouse development. *Developmental dynamics : an official publication of the American*
612   *Association of Anatomists* 242(10):1202-1209.

613

614

Figure legends:

616
617
618
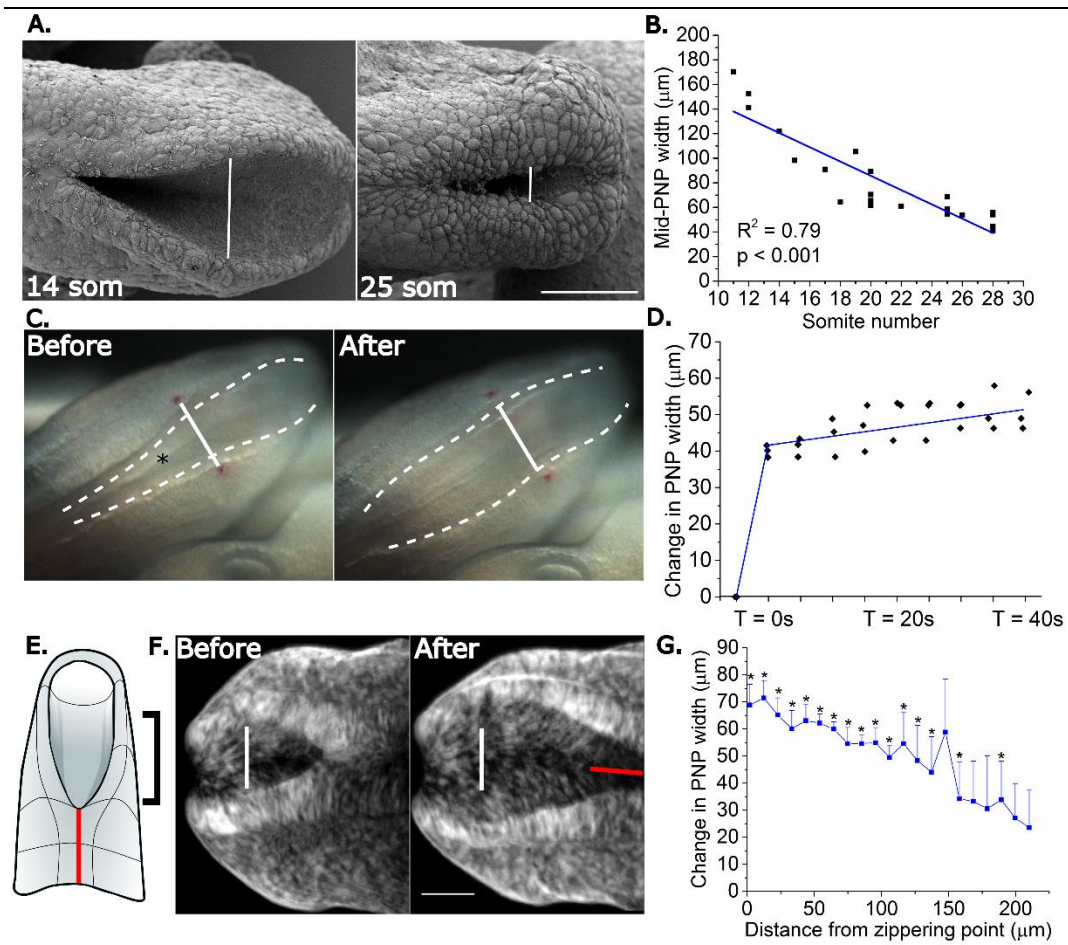
Figure 1: Midline apposition of the neural folds is opposed by mechanical tension.
A. Representative scanning electron micrographs of mouse PNPs at two stages of
development (somite stages indicated) showing the reduction in PNP width (solid lines) with
advancing stage. Scale bar = 100 μm. Rostral is to the left side, and caudal to the right. **B.**
Quantification of the width of the PNP at its mid-point at the indicated somite stages
demonstrating that the PNP gradually narrows as it closes. **C.** Representative images showing
widening of the PNP (dashed lines) following needle incision of the zippering point
(asterisk). The solid white line indicates distance between DiI labels before incision (See
supplementary video 1). **D.** Quantification of the change in PNP width (final − initial width)
at the indicated times following needle incision of the zippering point demonstrating that the
increase in PNP width occurs rapidly. **E.** Schematic illustration of the region ablated with
needle or laser (red line) and the approximate region in which widening of the open PNP was
quantified (black bracket). **F.** Representative images of a live-imaged embryo PNP before
and after laser ablation. The white line indicates PNP width before ablation; the red line
indicates the ablated NT region. **G.** Quantification of the change in PNP width following
completion of laser ablation (Z-stack capture was completed ~4 mins after ablation). The
change in width was measured every 10 μm caudally from the zippering point. PNP width
increases following ablation at least 200 μm caudal to the ablation site. Points represent the
mean ± SEM, n = 5 embryos. * $p < 0.05$ (width before versus after) by repeated measures
ANOVA with Bonferroni post-hoc.
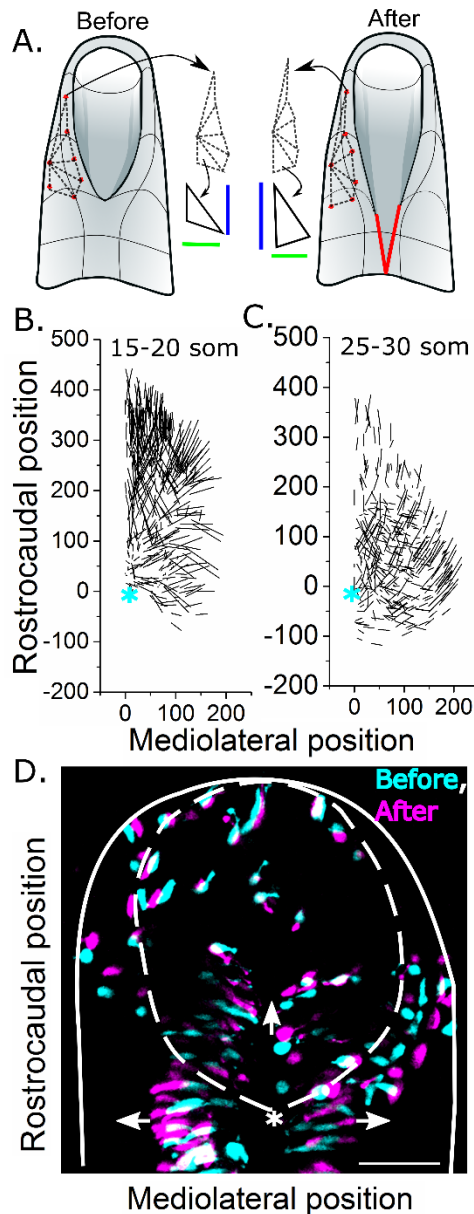
Figure 2: The PNP zippering point is under lateral and caudally oriented stresses. A. Schematic representation of the TDSM methodology (expanded in SI Appendix 1 Figure 1 and SI Appendix 2). Centroids of mosaic fluorescent cells (red dots) are linked 3-dimensionally in a Delaunay triangulation mesh. Changes in triangle dimensions are used to calculate strain. Displacement of the triangulation centroids provides displacement vectors. **B,C.** TDSM displacement analysis of (**B**) 15-20 somite and (**C**) 25-30 somite stage embryos illustrating 2D displacement vectors of triangulation centroids. Vector lengths indicate the magnitude of displacement and orientation indicates the direction of displacement following zippering point laser ablation (the zippering point at the origin, indicated by asterisks, is taken as the reference point). Data are shown as the aggregate of points from three embryos at each stage. **D.** Representative registered image of a 25 somite embryo in which fluorescent cells are produced via mosaic recombination of the mTmG transgene, driven by β-actin CreERT2. This illustrates the caudal and lateral displacement (arrows) of cells following zippering point (*) ablation relative to the zippering point (before ablation = cyan, after ablation = magenta). The outline of the PNP is indicated by the white dashed line. Scale bar = 100 μm.

656

657
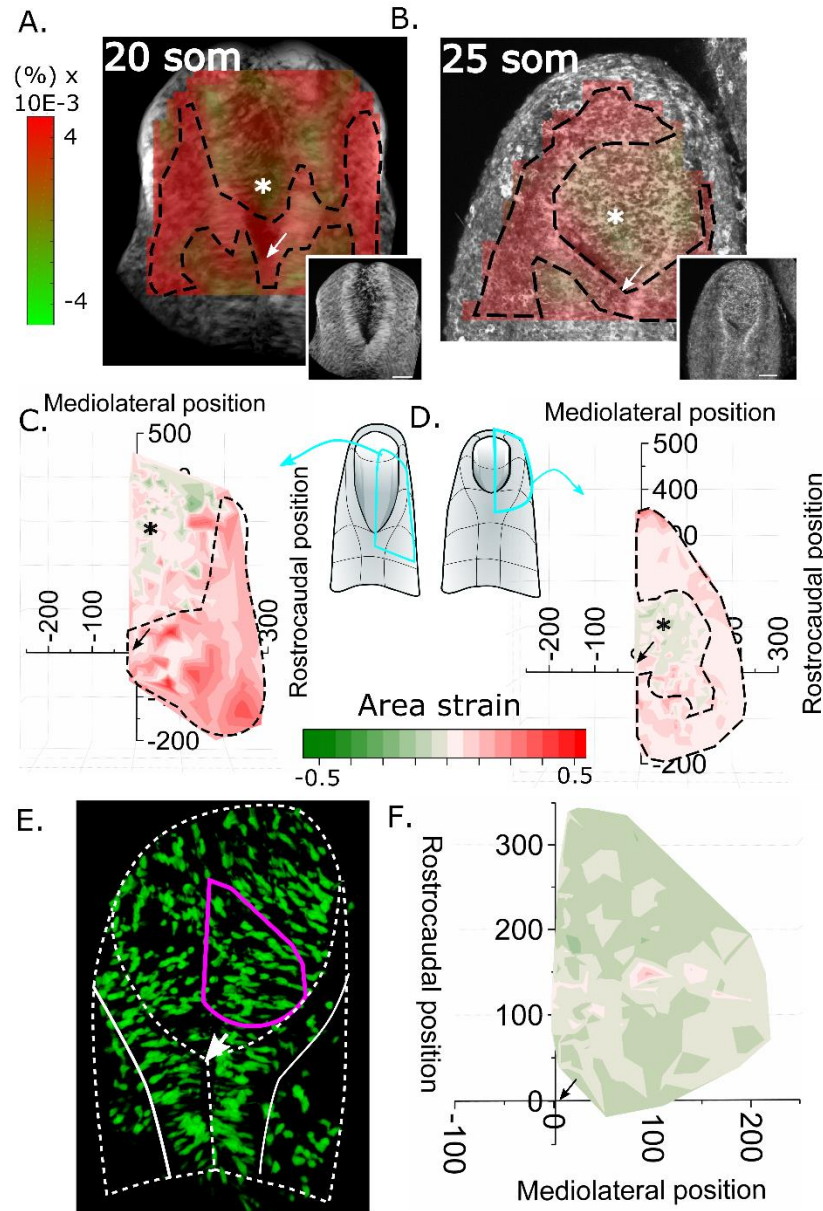
Figure 3: PNP zippering point ablation results in predominant tissue expansion around the zippering point and constriction of the NMP zone. A-D. Improved DIC von Mises strain maps (**A, B**) and TDSM area strain maps (**C, D**) of representative 15-20 somite (**A, C**) and 25-30 somite (**C, D**) embryos. These reveal tissue expansion (red, outlined with dashed lines) around the zippering point (arrows) and neural folds after ablation, whereas tissue compression (*) is predominantly observed caudal to the zippering point, in the midline NMP zone. **E.** Representative live-imaged posterior neuropore of a 20 somite Nkx1-2CreERT2; ROSA[YFP] mouse embryo illustrating the NMP zone region analysed by TDSM (magenta line) caudal and ventral to the zippering point (arrow). **F.** Area strain map selectively analysing Nkx1-2[CreERT2] expressing cells in the region shown in (**E**), confirming predominant tissue constriction (green) in this region following laser ablation of the zippering point (arrow), despite the previously demonstrated overall widening of the PNP. TDSM maps are in the orientations shown in the insets in A and B. While TDSM analyses are presented in 2D for publication purposes, they were all performed in 3D taking into account each cell's X, Y and Z centroid positions.

26
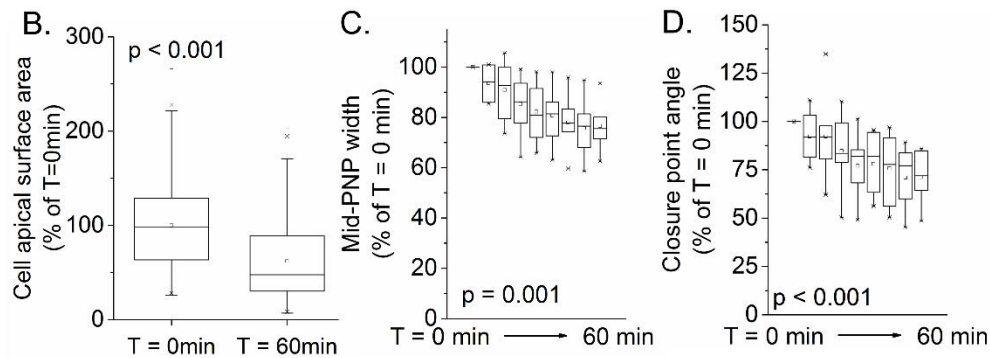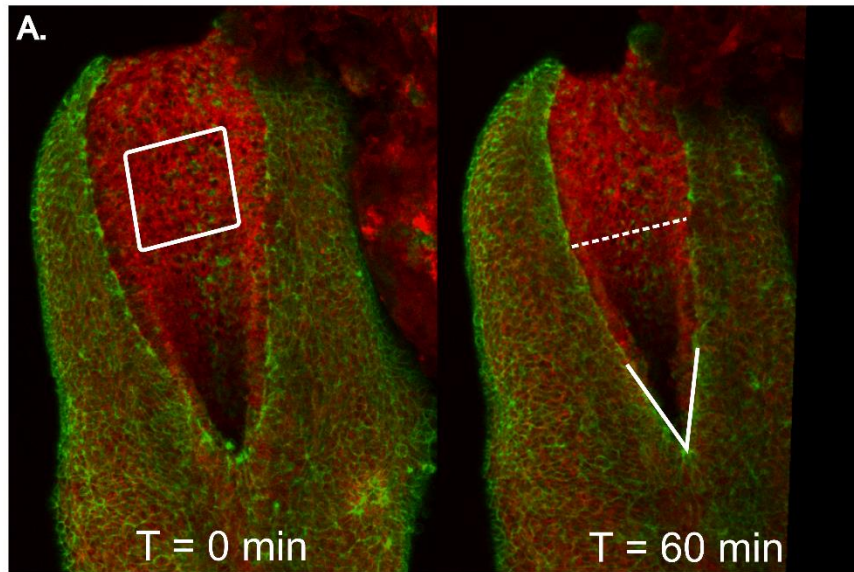
Figure 4: Neural fold midline apposition is associated with constriction of the NMP zone. A. Representative frames of a live-imaged Grhl3Cre; mTmG mouse embryo (~18 somites) at T = 0 min and T = 60 min (See supplementary video 2). The white box indicates the NMP zone, analysed in (**B**), the dashed line indicates mid-PNP width and the white "V" indicates the zippering point angle. **B.** Quantification of the apical surface areas in the NMP zone of live-imaged mTmG embryos based on tdTomato labelled membrane at T = 0 min and T = 60 min demonstrating a reduction in size consistent with apical constriction, a mechanism whereby the NMP zone may undergo constriction. Data represent 30 cell surface areas from each of 7 embryos. P value indicates difference between the two groups by Wilcoxon signed rank test. **C, D.** Quantification of the mid-PNP width (**C**) and zippering point angle (**D**) over 60 minutes of live imaging relative to the initial measurement for each embryo (T = 0 min set at 100%), n = 7. These analyses demonstrate the continued (or resumed) apposition of the neural folds and constriction of the NMP zone cells under live embryo imaging conditions. P values in **C** and **D** indicate significant change over time by mixed model analysis accounting for repeated measures from each embryo.
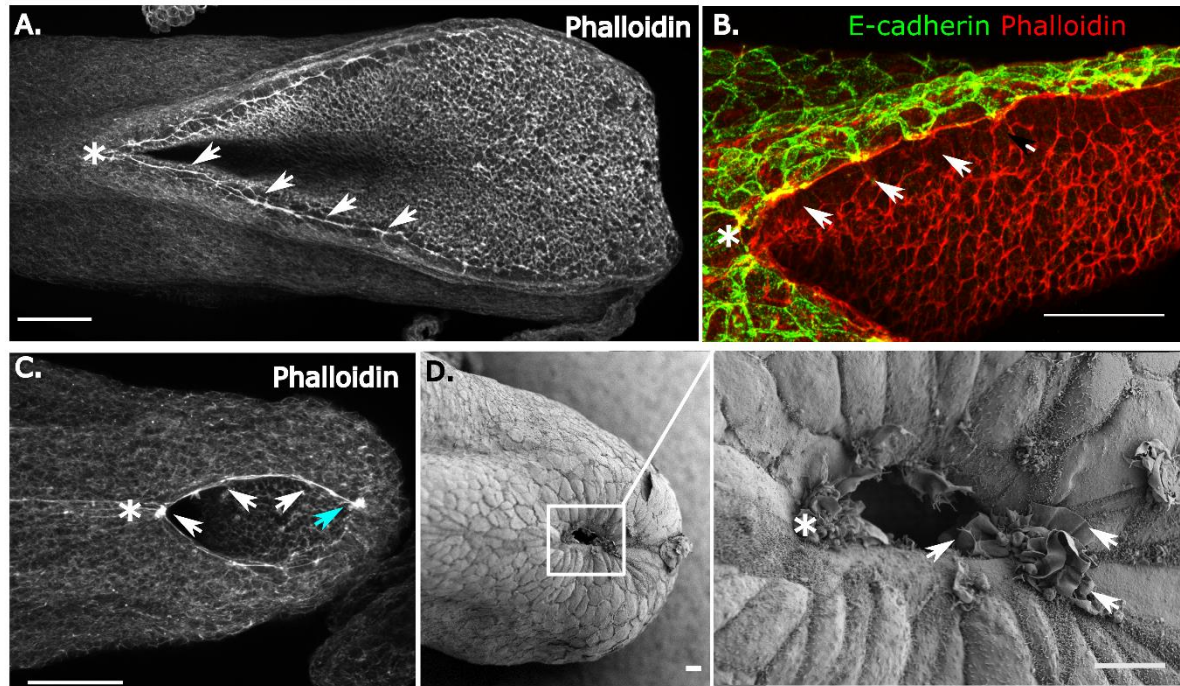
**Figure 5: A long-ranging F-actin network biomechanically couples the mammalian closing spinal neural tube. A.** PNP region of a representative 14 somite embryo stained with phalloidin to illustrate the presence of an F-actin cable (arrows) that runs caudally from the zippering point (*) along the closing neural folds. Scale bar = 100 μm. **B.** This cable at the surface ectoderm-neuroepithelial boundary co-localises with the surface ectoderm adherens junction marker E-cadherin (arrows). Scale bar = 20 μm. **C.** At later somite stages, when completion of PNP closure is imminent, this cable encircles the PNP (30 somite stage shown, cyan arrow indicates the caudal PNP canthus). Scale bar = 100 μm. **D.** At this stage, cellular protrusions are visible at the caudal extremity ('canthus') of the PNP (arrows in higher magnification SEM image on the right) as well as at the zippering point (asterisk). These features indicate formation of a new zippering point ("Closure 5"), as well as the continued presence of the original zippering point (*) at the rostral extremity of the PNP. Scale bars = 10 μm.
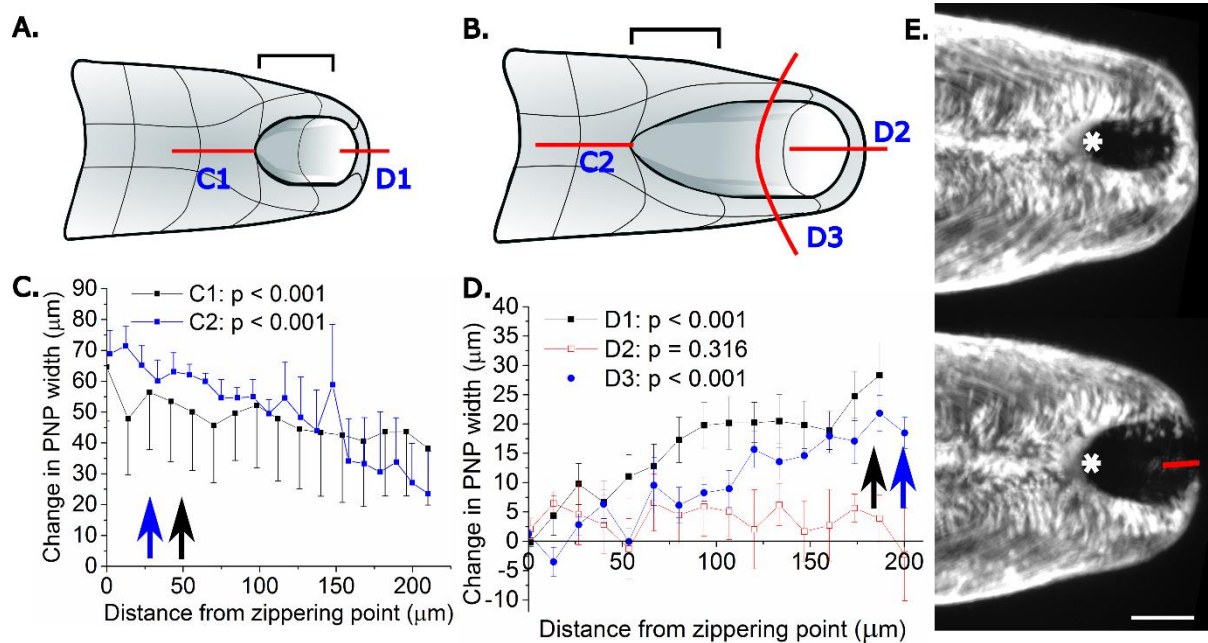
Figure 6: Laser ablation of the F-actin cable causes PNP widening. The F-actin cable was disrupted with a series of laser ablations. **A.** Two types of ablation were made in embryos at late somite stages (25-30 somites), when a complete F-actin ring has formed. The rostral extremity (zippering point, C1) or caudal extremity (closure 5, D1) of the PNP were ablated (red lines). **B.** Three types of ablations were made at earlier somite stages (15-20 somites). The zippering point was ablated (C2) as shown in Figure 1, caudo-ventral midline ablations paralleled the closure 5 ablations performed at later somite stages (D2), and the F-actin cable was ablated along the neural folds (D3). The ablations in the schematics are labelled to correspond with the analysis of changes in PNP width in the region indicated by the black brackets above each schematic. **C,D.** Change in PNP width at different positions along the PNP following ablations. The zippering point is at X = 0 in each graph. Zippering point ablation at both somite stages (C1/C2, n=5 in each case) results in PNP widening, most markedly near the zippering point (arrows) but also extending more than 200 μm caudally along the PNP. Ablations of closure 5 (D1, n=8) or through the neural folds (D3, n=6) increase PNP width caudal to the zippering point (arrows), whereas the zippering point itself was not disrupted. Caudo-ventral ablations before the formation of closure 5 (D2, n=4) did not significantly change PNP width (red line in D). P values indicate the overall differences comparing neural fold distance before versus after ablation, accounting for repeated measures from the same embryo at different rostro-caudal position by mixed model analysis. **E.** Representative frames of a live-imaged 29 somite embryo PNP before and after closure 5 ablation. Note the widening of the entire PNP after ablation. *=zippering point; red line=ablation; scale bar=100 μm.
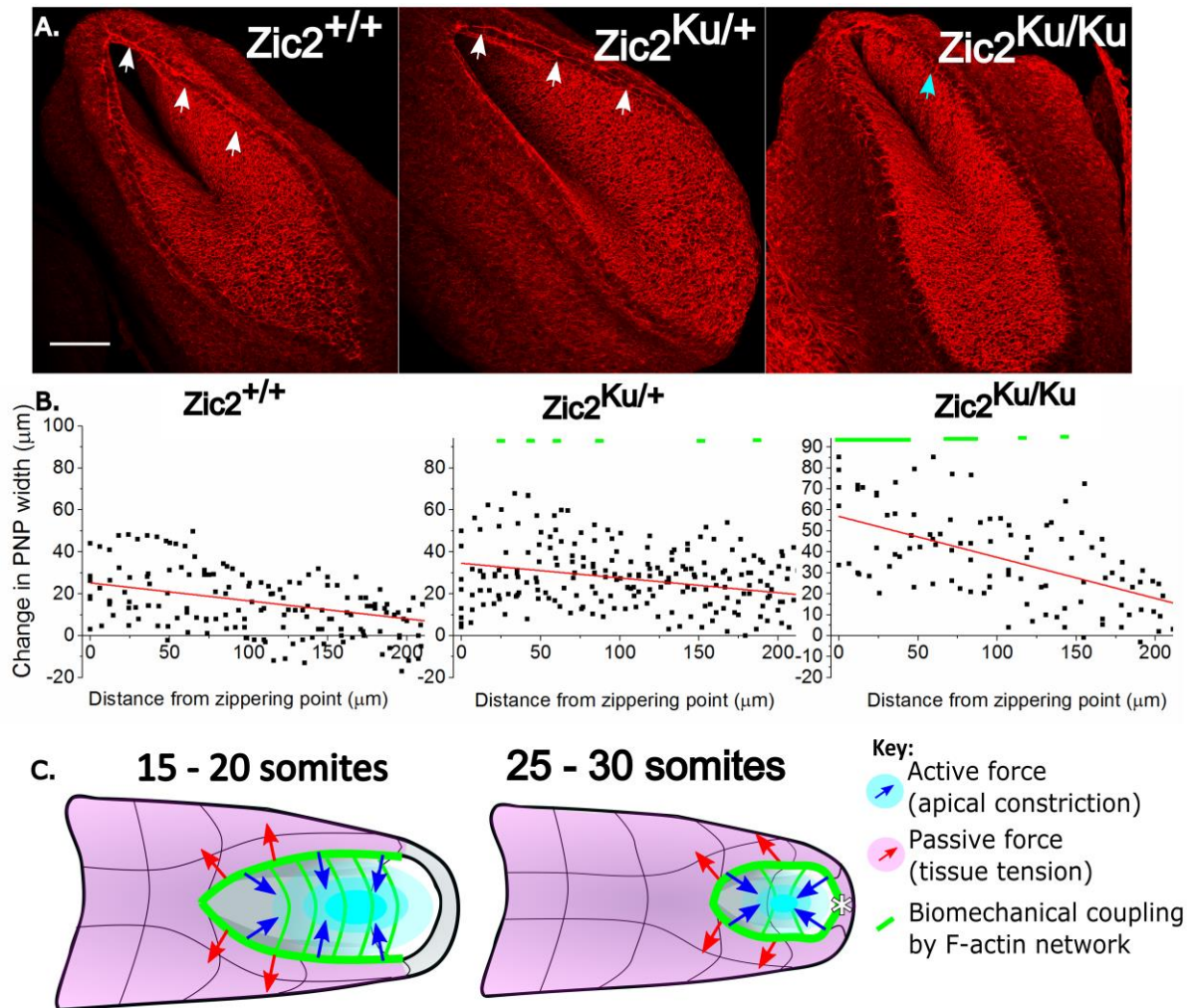
Figure 7: Zippering point ablation results in greater PNP widening in *Zic2^{Ku/Ku}* mutants than wild-type littermates. A. Whole mount phalloidin-labelled images of 13 somite wild-type, heterozygous and homozygous *Zic2^{Ku}* embryos illustrating the characteristic appearance of the PNPs. At this stage, PNP length is not significantly different between the three genotypes. Arrows indicate the F-actin cable, which is markedly less well defined in the *Zic2^{Ku/Ku}* genotype (cyan arrow). Scale bar = 100 μm. **B.** Quantification of the change in PNP width (final - initial width) at sequential positions caudal to the zippering point in embryos following zippering point laser ablation. Green lines indicate positions at which the *Zic2^{Ku/+}* (n = 8) or *Zic2^{Ku/Ku}* (n = 5) embryos showed significantly greater increases in width than *Zic2^{+/+}* littermates (n = 5). Individual distances from the zippering point were compared by Bonferroni post-hoc correction following mixed model analysis accounting for repeated measures from each embryo. Different symbols indicate values from different embryos. **C.** Schematic summary of the findings of this study. Constriction of the NMP zone (cyan) actively generates mechanical force (blue arrows) acting on the biomechanically coupled PNP. This opposes stresses within the surrounding tissues (red arrows), facilitating midline apposition of the neural folds, narrowing the zippering point angle and allowing zippering to progress. Encircling of the PNP by the F-actin cable (thick green line) and formation of Closure 5 (asterisk in right image) permits the caudal PNP canthus to biomechanically facilitate neural fold apposition when completion of closure is imminent.